Design and Simulation of a Vertical Waveguide Based Polarization Color Routing Device

F. Ali[1,2], B. Figeys[1], O. Shramkova[1], R. MacCiarnain[1], X. Rottenberg[1,3], R. Gehlhaar[1] and J. Genoe[1,2]

[1]*Imec, Kapeldreef 75, 3001 Leuven, Belgium*

[2]*KU Leuven, ESAT Department, Kasteelpark Arenberg 10 - bus 2440, 3001 Leuven, Belgium*

[3]*ULB, Ecole Polytechnique de Bruxelles, Av. Franklin Roosevelt 50, 1050 Brussels, Belgium*

Keywords: Color Routing, Polarization Routing, Vertical Waveguides, Image Sensors, Polarization-Dependent Imaging.

Abstract: We present a high index vertical-waveguide based optical device which offers polarization and color routing with sub-micron spatial resolution over the visible spectrum (400-700 nm). The device exploits a polarization, color splitting principle to effectively separate orthogonal linear polarization states, colors of the incident light beam respectively. Finite difference time domain simulations are performed to optimize the design parameters and analyse the device performance under different illumination conditions. The unique ability to simultaneously manipulate polarization and color with remarkable efficiency can allow a new era for high-resolution optical imaging devices.

1 INTRODUCTION

Image sensors are the backbone of modern imaging systems, which convert light into electrical signals, enabling the formation of a digital image equivalent. The pursuit of ultra-high resolution and high-quality imaging has driven significant advancements in image sensor technology, catering to a surging demand in an array of consumer and industrial applications such as smartphones, automotive systems, robotics, and surveillance (Park et al., 2022; Theuwissen A., 2021; Takahashi et al., 2017).

Conventional image sensors are comprised of a Bayer pattern color filter array to render color information for color images. These sensors generally detect only the intensity of the light but lack the ability to capture polarization data which can convey information about important characteristics and properties of the imaged scene. Nonetheless, incorporation of a polarization filter array into the image sensor allows for the realization of polarization-sensitive imaging, enabling a more comprehensive understanding of the captured scene (Gruev et al., 2010; Chen et al., 2016; Wu et al., 2023).

The functionality of these image sensors relies heavily on the filtering process, which unfortunately discards a substantial amount of light and reduces the signal-to-noise ratio, posing a major limitation to the pixel downsizing trend and thus hindering the continued miniaturization of imaging technology (Arbabi et al., 2018; Lee et al., 2023; Scott-Thomas J., 2023). To overcome this limitation, researchers have proposed several color and polarization routing devices, which split and direct the incident light into designated pixels based on spectral content and polarization state, without significant losses (Nishiwaki et al., 2013; Yun et al., 2021; Kang et al., 2023; Khorasaninejad et al., 2015; Rubin et al. 2019; Nesic et al., 2023). Although these approaches have successfully addressed the inherent efficiency limitations of filter-based image sensors, none of them have been able to integrate polarization and color splitting functionalities into a single device for highly-efficient polarization-dependent imaging.

In this paper, we demonstrate a design for simultaneous polarization and color routing to achieve a highly efficient polarization-sensitive image sensor. The proposed device comprises of vertical-waveguides and employs a splitting principle to achieve its intended functionality. Numerical simulations reveal that the device yields a total transmission efficiency of over 95%. Our design overcomes the long-standing efficiency limitations of traditional sensor designs, and boasts a compact footprint, with sub-micron pixel sizes making it a

Ali, F., Figeys, B., Shramkova, O., MacCiarnain, R., Rottenberg, X., Gehlhaar, R. and Genoe, J.
Design and Simulation of a Vertical Waveguide Based Polarization Color Routing Device.
DOI: 10.5220/0013121100003902

In *Proceedings of the 13th International Conference on Photonics, Optics and Laser Technology (PHOTOPTICS 2025)*, pages 15-19
ISBN: 978-989-758-736-8; ISSN: 2184-4364

suitable candidate for advanced optical imaging applications.

2 DESIGN AND SIMULATION

Figure 1 shows a schematic representation of the proposed polarization color router (PCR). A sketch of the unit cell design with a pitch P is depicted in Figure 1a. The PCR is composed of two optical components with distinct functionalities: a polarization splitter (PS) unit on top and color splitter (CS-X, CS-Y) unit below. Both units are composed of high index vertical-waveguides with TiO_2 as a core and a SiO_2 cladding. The corresponding geometric parameters and cross-sectional views are presented at multiple planes (A–D) along the propagation direction.

The primary function of the top PS is to route the input light beam to distinct output channels according to its polarization state. It comprises of two segments: a top square-shaped input waveguide (plane A) with thickness H2 and width W1, which tapers down asymmetrically to two partially overlapping orthogonal waveguides of dimension W1×W2 forming an L-shaped cross section at plane B. The bottom segment consists of an L-shaped waveguide of thickness H3, which gradually tapers down to two orthogonal square-shaped waveguides of width W2 (at plane C). The input waveguide adiabatically transmits the light beam to the L-shaped waveguide at plane B. Then, the beam is routed towards either of the square-shaped waveguides X or Y at exit plane of the PS (plane C), based on the incident polarization vector's orientation (horizontal or vertical polarization: indicated by green arrows).

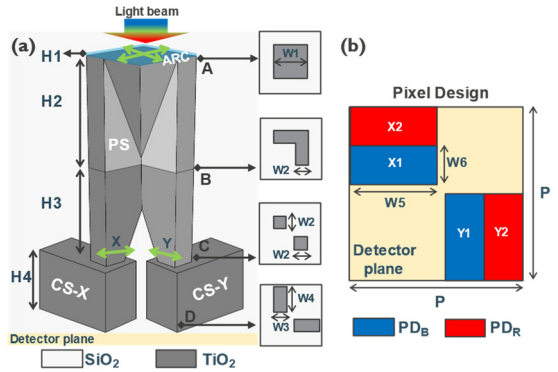

Figure 1: Schematic of the Polarization Color Router: (a) A unit cell design comprising vertical-waveguides with cross-sectional views at different planes. (b) A configuration for the pixel design at the detector plane for a unit cell with a pitch P = 1 µm.

Bottom color splitting elements (CS-X, CS-Y) separate the incident light signal into its constituent wavelengths or colors at sub-micron spatial resolution. To achieve this functionality multimode vertical-waveguides are employed, a technology previously validated in our earlier research (Kang et al., 2023). The color splitting segment consists of two identical rectangular waveguides with dimension W3 × W4 × H4, connected to the two orthogonal output channels of the top PS unit at plane C. The PS exit waveguide (X or Y) injects light asymmetrically into the color splitting element (CS-X or CS-Y), exciting both fundamental and second-order modes within the waveguide. As these modes propagate, their speeds vary with frequency causing spatial separation of colors at the waveguide exit (plane D). It is worth to mention, a subtle tuning of the waveguide's geometric parameters enables a precise control over the optimal color spectrum, demonstrating the versatility of our device. Finally, the separated colors (polarization dependent) are captured by corresponding pixels in the detector plane.

The device also features an H1 thick anti-reflection coating (ARC) layer on waveguide entrances to effectively reduce the back reflections and enhance device efficiency. When illuminated with a focused light beam from the top, device splits the beam into constituent color bands according to its polarization state, subsequently recorded in the relevant pixel. Here, the visible spectrum is divided into two bands (Blue/Red), with the potential to expand to three bands (RGB) by adjusting the waveguide's dimension. The proposed pixel design is composed of four pixels in a compact layout at the detector plane, labelled X1, X2, Y1, and Y2, with dimensions W5×W6, as shown in Figure 1b. The pixel pairs (X1, X2) and (Y1, Y2) are designed to capture blue and red spectral bands for X-polarized and Y-polarized light, respectively.

Finite difference time domain simulations in a commercial solver, were employed to perform a comprehensive optimization of design parameters and analyse the optical performance of PCR (Ansys Lumerical FDTD). A broadband Gaussian beam of numerical aperture (NA) 0.8 was used to excite the proposed device across the visible spectrum 400-700 nm. Unit cell simulations were performed with Bloch boundary conditions in X and Y directions, while perfectly matched layer (PML) boundary conditions were set for the Z axis (propagation direction). The optical constants of SiO_2 and TiO_2 used for simulations were taken from in-house measurements and presented in the Figure 2.

The optimal device parameters were determined through a two-stage nested sweeps simulation process, targeting maximum efficiency and low pixel cross-talk as main figure of merit. Initially, the top PS unit was optimized for maximum polarization routing efficiency, yielding optimal design parameters: P =1 µm, W1 = 550 nm, W2 = 200 nm, H2 = 2.8 µm, and H3 = 3.7 µm. Subsequently, optimization of color splitting elements enabled the separation of the polarization-routed beam into two spectral bands, leading to corresponding parameters: W3 = 200 nm, W4 = 400 nm, and H4 = 3.1 µm. ARC design principle and numerical optimization led to the selection of a 90 nm thick (H1) SiO_2 layer as the optimal anti-reflective coating. Meanwhile, subwavelength pixel dimensions of W5 = 225 nm and W6 = 500 nm were employed, yielding high spatial resolution.

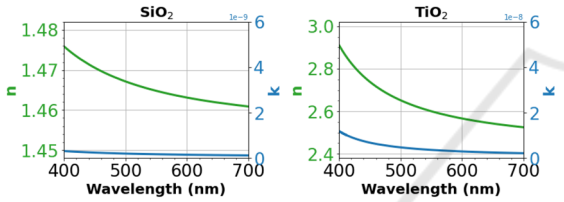

Figure 2: Material Optical Constants: Refractive Index (n, k) of SiO_2 and TiO_2.

3 RESULTS AND DISCUSSION

Figure 3 shows the simulated optical performance of the proposed device under broadband visible illumination (400-700 nm). The simulated electric-field intensity distribution at the detector plane is presented in Figure 3a, showing the device's response to blue (450 nm) and red (650 nm) wavelengths for both X and Y polarization states. For X-polarization, the incident light is primarily directed to the X output channel at the PS exit (plane C: Figure 1a), then routed to the CS-X splitting element where blue and red wavelengths propagate at different speeds and are separated into X1 and X2 pixels as evident from the top row of Figure 3a. In contrast, Y1 and Y2 capture the aforementioned colors for the orthogonal (Y) polarization state (bottom row). Meanwhile, it is worth to mention that for all four possible configurations, the field is highly localized in the designated pixels ensuring high efficiency with minimal polarization and color crosstalk.

Figure 3b shows the spectral response of the PCR for orthogonal polarization states of the incident light beam. It can be observed that for X-polarization, the majority (≈50%) of light in the blue band (400-550 nm) is collected by the X1 pixel, meanwhile X2 captures the red band (550-700 nm) with a similar efficiency. The geometric symmetry induces a similar response for the orthogonal polarization state (on the right side of Figure 3b but now with Y1 and Y2 active pixels. Average cross-talk between the active pixels across the two spectral bands is 35-40%, which can be further supressed by introducing deep trench isolation (DTI) between the pixels. The device achieves remarkable efficiency, featuring high (>95%) total transmission and low (<5%) reflection. Moreover, the device exhibits a low power leakage, with under 5% of power directed to pixel-free region.

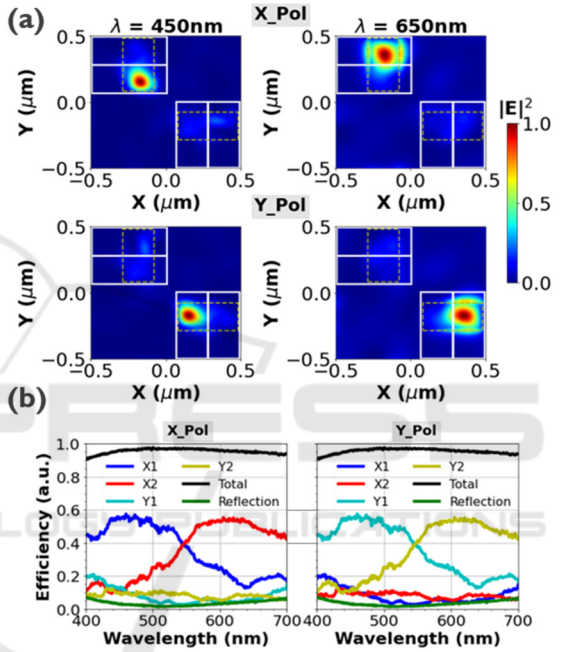

Figure 3: Optical performance of the PCR: (a) Normalized electric-field intensity distribution profiles at the detector plane for orthogonal polarization states (X and Y) at 450 nm and 650 nm. The white (solid) and yellow (dashed) rectangles define the four pixel and bottom color splitters perimeters. (b) Transmission and reflection efficiency for X and Y-polarized incident light over the visible spectrum.

Next, we demonstrate the device's versatility by tuning the short-axis width (W3) of color splitting units (CS-X, CS-Y) to support multiple color compositions. For this purpose, simulations were performed by sweeping W3 from 150 nm to 250 nm, using an X-polarized Gaussian beam (NA = 0.8). Figure 4 illustrates the dependance of pixel (X1, X2) transmission efficiency over incident beam's wavelength and waveguide's short-axis width. These transmission maps indicate a gradual shift of the crossing point (identified by black arrows) of two separated spectral bands, defining the color

information in the relevant pixel. With a short-axis width of 150 nm, wavelengths between 400-500 nm were directed to pixel X1 and X2 received 500-700 nm, whereas the 250nm width split the spectrum into 400-570 nm (X1) and 570-700 nm (X2), without any significant loss in the routing efficiency. Thus, by precise control over short-axis width, the desired color composition can be achieved. Furthermore, tailoring thickness (H4) and long-axis width (W4) can offer additional degree of freedom to achieve customized spectral splitting.

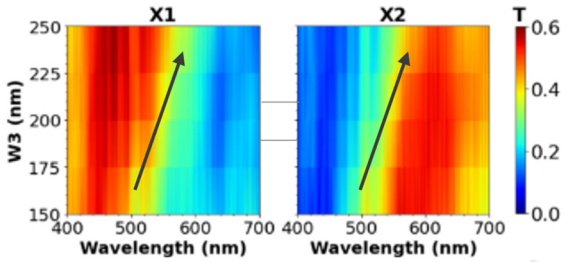

Figure 4: Variation of pixel's spectral composition: Power transmission to the X1 and X2 pixel as a function of wavelength and short axis width of bottom color splitting unit.

To analyze the device's capability to operate under different illumination conditions, it was excited with an X-polarized Gaussian beam by varying the numerical aperture between 0.1-0.9. Figure 5 depicts the power routed to the corresponding pixels (X1, X2) as a function of wavelength and numerical aperture. It is evident that the device performs as intended and separates the two wavelength bands (blue and red) for all illumination numerical apertures, albeit with changes in efficiency. Although, pixel's transmission efficiency drops as NA decrease, yet remains ≈25% for the lowest designed NA of 0.1. Nonetheless, we anticipate that by following the optimization process, the device can be tailored to operate at desired NA with high routing efficiencies.

Further investigation will focus on expanding the device's capabilities to separate polarization-dependent visible light into red, green, and blue (RGB) spectral bands by tailoring the color splitting waveguide's geometric dimensions. While the bottom color splitters have already been successfully fabricated using standard backend processing techniques on 300 mm wafers (Kang et al., 2023), we will explore advanced lithography and fabrication techniques to develop top polarization splitting waveguides to realize complete device stack. Ultimately, optical characterization will be performed to determine the device's true efficiency and validate its performance.

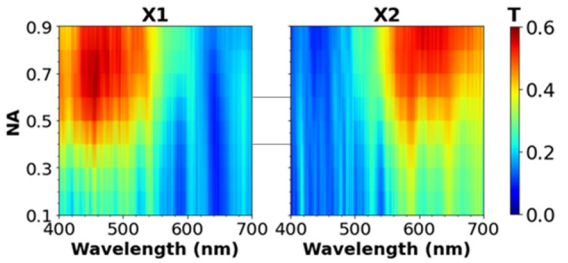

Figure 5: Device performance under a wide range of illumination numerical aperture (NA) settings: Power transmitted to the X1 and X2 pixel as a function of designed numerical aperture and wavelength.

4 CONCLUSION

In conclusion, a novel high index vertical-waveguide based polarization color routing device at visible wavelengths is proposed and investigated through numerical simulations. The key innovation lies in simultaneously splitting the polarization and color at sub-micron spatial resolution with near unity transmission and a high pixel routing efficiency of 50%. The design's versatility enables a tuneable color composition via geometric parameter modulation and adoptability to perform well over a wide range of numerical aperture settings. We firmly believe this device shows great promise to be implemented for high NA polarization-sensitive image sensors with possible applications in high-end professional cameras, smartphones, and machine vision devices.

REFERENCES

Park, S., Lee, C., Park, S., Park, H., Lee, T., Park, D., Heo, M., Park, I., . . . & Kim, T. (2022). A 64Mpixel CMOS Image Sensor with 0.56μm Unit Pixel Separated by Front Deep-Trench Isolation. IEEE International Solid-State Circuits Conference (ISSCC), San Francisco, CA, USA, pp. 1-3. https://doi.org/10.1109/ISSCC42614.2022.9731750.

Theuwissen A. (2021). There's More to the Picture Than Meets the Eye, and in the future it will only become more so. IEEE International Solid-State Circuits Conference (ISSCC), San Francisco, CA, USA, pp. 30-35. https://doi.org/10.1109/ISSCC42613.2021.936605.

Takahashi, S., Huang, Y-M., Sze, J-J., Wu, T-T., Guo, F-S., Hsu, W-C., . . . & Yaung, D-N. (2017). A 45 nm Stacked CMOS Image Sensor Process Technology for Submicron Pixel. Sensors, 17(12), 2816. https://doi.org/10.3390/s17122816.

Gruev, V., Perkins, R., & York, T. (2010). CCD polarization imaging sensor with aluminum nanowire

optical filters. Opt. Express 18, 19087-19094. https://doi .org/10.1364/OE.18.019087.

Chen, W. T., Török, P., Foreman, M. R., Liao, C. Y., Tsai, W-Y., Wu, P. R., & Tsai, D. P. (2016). Integrated plasmonic metasurfaces for spectropolarimetry. *Nanotechnology 27 224002*. https://doi.org/10.1088/0957-4484 /27/22/224002.

Wu, Y., Yang, Y., Yin, Y., Dai, L., Li, X., Huang, H., & Wen, S. (2023). Flexible high-resolution thin micropolarizers for imaging polarimetry. *Chin. Opt. Lett. 21, 031301*. https://doi.org/10.3788/COL202321 .031301.

Arbabi, E., Kamali, S. M., Arbabi, A., & Faraon, A. (2018). Full-Stokes Imaging Polarimetry Using Dielectric Metasurfaces. *ACS Photonics, 5 (8), 3132–3140*. https://doi. org /10.1021/acsphotonics.8b00362.

Lee, G-D. R., Kim, D-H., Kwon, D., Park, J-E., Cho, D., Kang, J., . . . & Song, J. (2023). A 0.5μm Pixel 3-layer Stacked CMOS Image Sensor with Deep Contact and In-pixel Cu-Cu Bonding Technology. *International Electron Devices Meeting (IEDM), San Francisco, CA, USA, pp. 1-4*. https://doi.org/10.1109/IEDM45741. 2023.10413687.

Scott-Thomas, J. (2023). Trends and Developments in State-of-the-Art CMOS Image Sensors. https://www.imagesensors.org/Past%20Workshops/2023%20Workshop/2023%20Papers/R1.pdf

Nishiwaki, S., Nakamura, T., Hiramoto, M., Fujii, T., & Suzuki, M. (2013). Efficient colour splitters for high-pixel-density image sensors. *Nature Photon, vol. 7, no. 3, pp. 240–246*. https://doi.org/10.1038/nphoton. 2012.345.

Yun, S., Roh, S., Lee, S., Park, H., Lim, M., Ahn, S., & Choo, H. (2021). Highly Efficient Color Separation and Focusing in the Sub-micron CMOS Image Sensor. *IEEE International Electron Devices Meeting (IEDM), San Francisco, CA, USA, pp. 30.1.1-30.1.4*. https://doi.org/10.1109/IEDM19574.2021.9720592.

Kang, S., Benelajla, M., Ciamain, R. M., Ali, F., Papadopoulou, A., . . . & Genoe, J. (2023). Wafer-level-integrated vertical-waveguide sub-diffraction-limited color splitters. *International Electron Devices Meeting (IEDM), San Francisco, CA, USA, pp. 1-4*. https://doi.org/10.1109/IEDM45741.2023.10413746.

Khorasaninejad, M., Zhu, W., & Crozier, K. B. (2015). Efficient polarization beam splitter pixels based on a dielectric metasurface. *Optica 2, 376-382*. https://doi.org /10.1364/OPTICA.2.000376.

Rubin, N. A., D'Aversa, G., Chevalier, P., Shi, Z., Chen, W. T., & Capasso, F. (2019). Matrix Fourier optics enables a compact full-Stokes polarization camera. *Science365, eaax1839*. https://doi.org/10.1126/science .aax1839.

Nesic, A., Blaicher, M., Marin-Palomo, P., Füllner, C., Randel, S., Freude. W., & Koos, C. (2023). Ultra-broadband polarisation beam splitters and rotators based on 3D-printed waveguides. *Light: Advanced Manufacturing 4, 23*. https://doi.org/10.37188/lam. 2023.022.

Ansys Lumerical FDTD. https://www.ansys.com/products /optics/fdtd.